Soft Matter

Deformation-dependent polydimethylsiloxane permeability measured using osmotic microactuators

Journal:	*Soft Matter*
Manuscript ID	SM-ART-12-2022-001666.R1
Article Type:	Paper
Date Submitted by the Author:	13-Jul-2023
Complete List of Authors:	Spitzer, Alexandra; University of Illinois at Urbana-Champaign, Materials Science and Engineering Hutchens, Shelby; University of Illinois at Urbana-Champaign, Mechanical Science and Engineering; University of Illinois at Urbana-Champaign, Materials Science and Engineering

Soft Matter

ARTICLE TYPE

Cite this: DOI: 00.0000/xxxxxxxxxx

Deformation-dependent polydimethylsiloxane permeability measured using osmotic microactuators†

Alexandra R. Spitzer[a] and Shelby B. Hutchens[a,b,*]

Received Date
Accepted Date

DOI: 00.0000/xxxxxxxxxx

In soft solids, large deformations significantly alter molecular structure and device geometry, which can impact other properties. In the case of mass transport, an interplay between flux and mechanical deformation results. Here we demonstrate a platform for the simultaneous characterization of mechano-permselectivity using the (slow) transport of water through polydimethylsiloxane (PDMS) as a challenging test case. The platform uses micron-sized, cylindrical, NaCl solution-filled PDMS chambers encapsulated by selectively-permeable PDMS thin film membranes. When placed in a high chemical potential environment (high water potential) the osmotic pressure difference between the chamber and environment induces water to flow through the PDMS membrane into the chamber, resulting in membrane bulging. A model combining membrane flux and nonlinear elasticity captures the time-dependent response well, but only when a deformation-dependent permeability is used. Notably, the permeability of water through PDMS decreases by nearly an order of magnitude, from 2×10^{-12} to 5×10^{-13} m^2/s, due to primarily to its thickness decreasing by nearly an order of magnitude as the average biaxial stretch increases from 1 to 2.75.

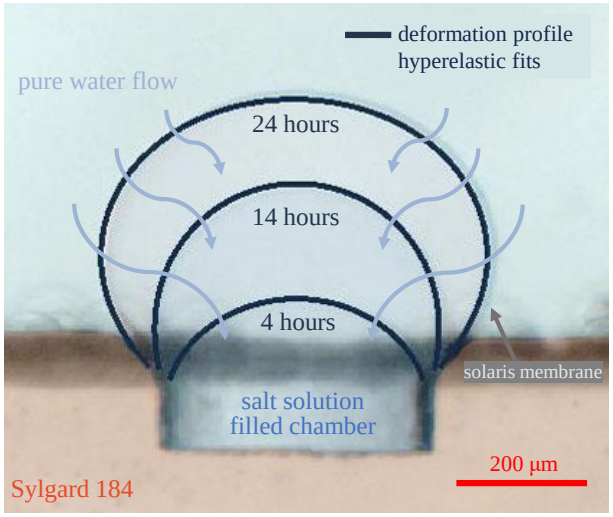

Fig. 1 Overlayed, time-lapse optical images of a bulging membrane in cross-section at 4, 14, and 24 h. Dark blue curves are deformation profile *fits* of a nonlinear bulge model employing the Gent 3-parameter strain energy density function.

1 Introduction

Membrane permeability determines fluid transport in industrial separations,[1–4] biological function,[5–11] and bio-inspired technologies.[12–19] Frequently, permeability is quantified under rigid, static conditions. However, in soft biological materials and bio-inspired devices, large changes in geometry and/or stretch occur, leading to an interplay between fluid transport and mechanical response that can be central to function. Observations and models of materials'[20–22] and tissues'[23–25] poroelastic response abound in hydrated and porous materials, for which transport is governed by Darcy's law. Yet few methods to measure the mechano-transport properties in materials exhibiting a solution-diffusion mechanism have been reported.[26–29] Here, we demonstrate a small-scale, bulge-based test platform for quantifying membrane mechano-permselectivity. Using this approach, we evaluate the deformation-dependent permeability of water within commercial polydimethylsiloxane (PDMS), an elastomer known for its biocompatibility and high stretchability as well as its separations properties (*e.g.*, pervaporation[30]). This small-scale approach resolves small flux volumes, which are particularly challenging to measure in membranes with extremely low permeability, including water through PDMS.

Previous investigations of water permeability within PDMS find that it is low and dependent on network structure, but its deformation or geometry-dependence has not been described. However, for gas and vapor permeants (CO_2, H_2, and H_2O),

[a] *Department of Materials Science and Engineering, University of Illinois Urbana-Champaign, Urbana, IL, USA.*
[b] *Department of Mechanical Science and Engineering, University of Illinois Urbana-Champaign, Urbana, IL, USA. E-mail: hutchs@illinois.edu; Tel: +1 (217)300-0412*
† Electronic Supplementary Information (ESI) available: : Nine pages of supplementary text and figures. See DOI: 10.1039/cXsm00000x/

PDMS reportedly becomes *thickness* dependent below tens of microns.[31,32] The behavior is attributed to non-equilibrium sorption-desorption processes at the interface, which take over as the dominant flux-limiting mechanism for sufficiently thin films.[33]

A membrane's microstructure can also regulate its permeability[34] via structural contributions to both the sorption of a solution *into* the membrane and subsequent diffusivity *within* it.[35,36] Under load, polymeric membranes experience deformation that modifies that microstructure. Consistent with other polymeric membrane systems,[27,37,38] PDMS's permeability to water vapor has been found to decrease as the chain mobility decreases;[29] mobility was controlled by changing crosslink density and verified with its proportionality to the glass transition temperature. Notably, Song, et al.[39] reported stretch dependent permeability of *ethanol* through PDMS. However, the mechanism used to capture the response derives from changes in hydraulic resistance to flow within channels in the network. Such channels are possible for ethanol, since ethanol slightly swells PDMS by 4%.[40] However, PDMS is known to be highly hydrophobic, exhibiting swelling of $\sim 0.1\%$,[41] which could *at most* yield submicron channels that would deviate from typical hydraulic behavior. The results we present here suggest a potentially minor effect of material stretch on permeability for this PDMS system and a description of stretch-dependent permeability in non-swelling network solids is outside the scope of the current work.

Our experimental design employs an osmolyte-filled chamber and a deformable, selectively permeable membrane that bulges as fluid enters (Fig. 1). Modeling chamber dynamics necessitates combining 1) membrane-mediated, osmosis-driven flow, 2) variable membrane surface area and thickness (in contrast to devices that separate actuation and permeability functions) and 3) nonlinear mechanical constitutive behavior.[42–46] Our approach to these requirements combines the following previous work. In describing the capabilities of osmotic actuators, Sinibaldi et. al.[13,14] modeled the volumetric actuation, characteristic actuation time, maximum applied force, and peak power of a bulging membrane under the assumption of *linear* elasticity attached to a large, *rigid*, osmotically-active chamber (fixed permeable surface area and thickness). The device is theoretically reversible.[47] We modify their framework to achieve the second point above by predicting chamber geometry changes via nonlinear membrane mechanics (third point). Experimental characterization of the deformation of pressurized hyperelastic membranes has been successfully captured by both analytical[48–50] and finite-element models.[51,52] Interestingly, while bulge deformation profiles are reported, model validation typically compares pressure to a single parameter, applied fluid volume[48] or maximum membrane displacement.[49,51,52] Here we show agreement between the hyperelastic membrane model[53] and the *entire bulge profile*, strengthening the flux model fidelity and therefore the argument for a varying permeability during actuation.

The article is organized as follows. First, we describe the materials and methods. Next, we discuss the principles driving chamber operation. Membrane mechanics comprise a key input of the modeling framework, and we provide solutions for both linear elastic and hyperelastic materials. Finally, the model is compared with the experimental time-dependent response. As a proof-of-concept, we report on the effects of incorporating hydrophilic components within the PDMS membrane to increase its sorption coefficient and therefore permeability.

2 Materials and Methods

Using a soft lithography approach, we form NaCl-filled chambers encapsulated by thin PDMS films.

2.1 Materials

We use two commercially available PDMS formulations (Sylgard 184, Solaris) and one PDMS-based composite (PEO-Solaris).

Sylgard 184, cylindrical chamber base. Sylgard 184 (Dow Corning) in a 10:1 (wt:wt) ratio, prepolymer base to curing agent is mixed for 45 s at 2500 RPM in a SpeedMixer (Flactek, Inc.)

PDMS (Solaris), membranes. Solaris (Smooth-On, Inc.) parts A and B are mixed in a 1:1 (wt:wt) ratio for 45 s at 2500 RPM in the SpeedMixer.

PEO-PDMS (Solaris), membranes. PDMS composite membranes are composed of allyloxy polyethylene oxide (PEO) (GELEST, INC.) and Solaris. Following previous work,[54] a 10:1 (wt:wt) dichloromethane (DCM) (Fisher) to polyethylene oxide (PEO) (GELEST, INC.) solution is hand mixed for 1 min. DCM-PEO is added to uncured Solaris at a ratio of 1.25 g of DCM-PEO per 25 g Solaris (5000 ppm (by mass) PEO), mixed for 45 s, at 2500 RPM (SpeedMixer), then degassed in a vacuum chamber.

2.2 Device Fabrication

Cylindrical well-structures in Sylgard 184 are immersed in NaCl solution. Elastomeric membranes consisting of a cured/uncured bilayer are adhered to the immersed structures, thereby encapsulating solution within the chambers.

PDMS Chamber Fabrication. Sylgard 184 chambers are molded (30 min degas; 70°C cure; 1.5 h) from a photolithographically patterned[55] micropillar mold. The mold is comprised KMPR 1010 negative photoresist (Microchem) micropillars of radii ranging from 100-200 μm and a height of 110 μm.

Selectively Permeable Membrane Fabrication. Solaris and PEO-Solaris membranes are spun coat (Laurell Technologies) on glass slides. First, polyacrylic acid (PAA) (Sigma Aldrich) and reverse osmosis (RO) water solutions (Table 1) are deposited at 1000 RPM for 40 s, to serve as a sacrificial layer. Films are placed on a hotplate at 100°C for 1 min to cure and eliminate excess water. Then PDMS is deposited twice; the first layer is cured (70°C for 1 h) and the second left uncured to serve as an adherent. Each layer is spun for 5 min according to the information in Table 1.

Structure Assembly. We test 5 or more devices for each of the following experimental configurations: reference chamber ($a = 200$ μm, $l_0 = 20$ μm, $h = 110$ μm, and $C_0 = 3$ M), small radius chamber ($a = 100$ μm), thick membrane chamber ($l_0 = 26$ μm), reduced osmotic loading chamber ($C_0 = 1$ M), and PEO-PDMS membrane chamber ($a = 200$ μm, $l_0 = 20$ μm, $h = 110$ μm, and $C_0 = 3$ M) where unspecified conditions match the reference chamber. Before assembly, the NaCl solution (3

Table 1 Selectively-permeable Membrane Spin Coating Process Conditions

Membrane	PAA Solution (wt.%)	Cured Layer Speed (RPM)	Adherent Layer Speed (RPM)	Membrane Thickness (μm)
Solaris	5	3000	2500	20
Solaris	5	2000	2000	26
PEO-Solaris	15	3000	2500	20

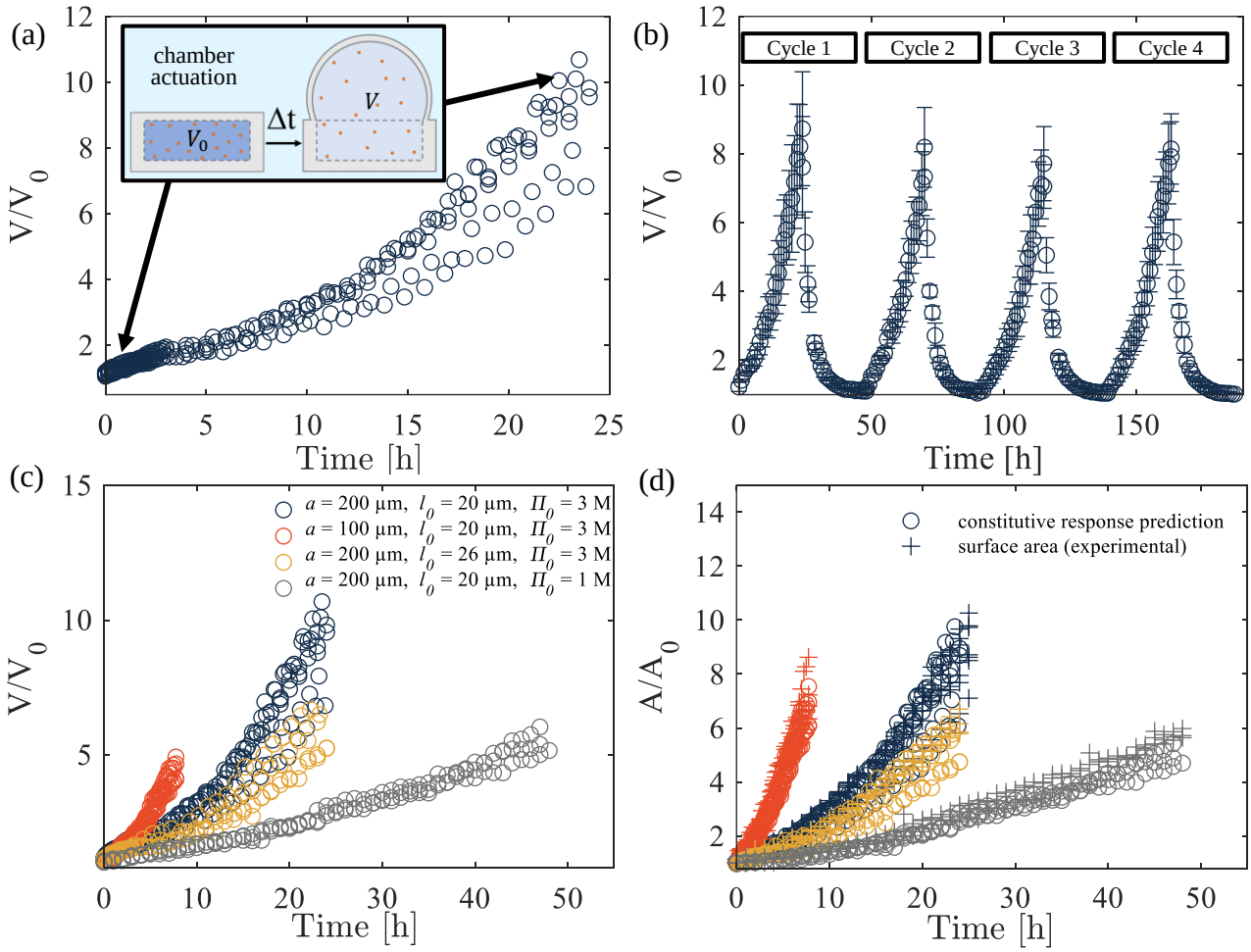

Fig. 2 Normalized actuation response of microchambers over time. (a) The normalized volume V/V_0 of the reference chamber ($a =$ 200 μm, $l_0 =$ 20 μm, $C_0 =$ 3 M) exhibits a nonlinear time-dependent response (7 samples). (b) Reversible reference chamber actuation across 4, 48 h cycles indicate negligible salt leakage over this time scale. (c) Four actuation chamber conditions are investigated in this work: the reference conditions (navy blue, same as (a)), a small radius chamber: $a =$ 100 μm (orange), a thick membrane chamber: $l_0 =$ 26 μm (gold), and a reduced osmotic loading chamber: $C_0 =$ 1 M (gray). (Unlisted parameters match the reference.) (d) Actuation response expressed as membrane surface area ratio $\frac{A}{A_0}$ over time is equivalent to V/V_0. For the four actuation chamber conditions in (c), direct experimental measurement (crosses) and conversion from V/V_0 (as plotted in (c)) using the mechanical bulge model (circles) provide similar results.

or 1 M solutions in RO water) is degassed for 30 min to pull water into the wells. Membrane assemblies are fixed to a test stand mounted (TA.XT Plus 100, StableMicrosystems) cylindrical compression probe and brought into contact with the submerged chambers at a rate of 1 mm/min to a pressure of 50 kPa. The structure is held in compression for 12 h, curing the adherent layer and dissolving the PAA layer.

2.3 Imaging and Analysis

Optical micrographs of the device cross-section (Fig. 1) are taken every 10-15 min over a span of 24 h (AxioObserver, Zeiss). Custom MATLAB code fits an elliptical curve to each membrane deformation profile from which volume change is determined via integration.

2.4 Mechanical Characterization

We characterize mechanical response by simultaneously fitting the bulge geometry in the previous section and a standard uniaxial test geometry.

Uniaxial Tension. We fabricate tensile specimens with 'dogbone' geometries (ASTM D412-16, die type D) and load them at a strain rate of 0.03 s^{-1}, using optical strain quantification (fiducial markers) until rupture (5 kg load cell).

3 Results and Discussion

The following results demonstrate the necessity of a deformation-dependent PDMS water permeability, arising from the inability of a time-dependent flux model with *constant permeability* to accurately capture experimentally-observed chamber volume evolution. This shortcoming occurs despite accurate accounting of finite deformation mechanics in the microactuator's response.

3.1 Bulging of Osmotically-Active Chambers

Driven by an osmotic pressure difference, pure water in the environment permeates the thin membrane into the salt-water-filled chambers, deflecting the membrane to accomodate the increased chamber volume (Fig. 1). Mechanical equilibrium requires that the hydrostatic pressure within the chamber increase to support the bulging membrane. The increase in hydrostatic pressure P_t and the decreased magnitude of the osmotic potential Π ($\Pi < 0$ for finite salt concentration) combine to increase the chamber water potential Ψ. Ψ quantifies the driving force for water movement, where water flows from regions of high to low potential. For pure water at atmospheric pressure, $\Psi = 0$ (ESI†). We calculate the total volume of water in the chamber V from the bulged profile assuming cylindrical symmetry. Fig. 2a illustrates the normalized time-dependent evolution of the chamber volume V/V_0 for a set of chambers in what we refer to as the reference configuration (chamber radius $a = 200$ μm, initial membrane thickness $l_0 = 20$ μm, chamber height $h = 110$ μm, and initial salt concentration $C_0 = 3$ M). This data was gathered to the point at which observation was hindered by: membrane delamination, membrane fracture, or interference between bulges. Despite slow permeability in silicone membranes, volume increases by a factor of 8 over 24 h due to the actuator's small size.

Two key benefits accompany the day-length timescale of actuation. First, within the microscale chamber, both solute and solvent diffuse across the entire chamber within approximately 3 s (ESI†). This separation of local mixing and macroscopic deformation time scales means the chamber can be considered well-mixed and concentration polarization does not occur. Additionally, the process is quasi-static, thus we ignore viscoelastic effects. These features provide the basis for many of the assumptions used in the model to follow.

The membrane bulges due to water flow through the membrane, so it is possible the osmolyte could permeate, resulting in salt leakage. To quantify salt-leakage, we actuate these membranes through four cycles. Forward actuation (bulging) is induced by submerging devices in pure RO water, causing water to flow through the membrane in a response to the lower water potential inside the chamber. After 24 h of forward actuation, the feed solution is replaced with a solution isotonic to the initial chamber solution and reverse actuation commences for 24 h due to a reversal of water potential. As Fig. 2b shows, observations across four cycles reveal no significant difference in maximum actuation, unactuated state, or time-scale of actuation. With these results as motivation, we make the assumption that on the timescale of these studies, no significant salt leakage occurs.

Qualitatively, variations in actuator parameters yield anticipated trends. As shown in Fig. 2c, a smaller chamber radius a increases the rate at which actuation occurs (increased V/V_0 vs. t slope, orange) and a thicker membrane l_0 and lower initial salt concentration C_0 decrease the rate at which it occurs (gold and gray data, respectively). (All chambers have the same 110 μm depth.) We validate the model developed in the following section by quantitatively capturing all of these responses using a single permeability function.

The membrane area and thickness increase and decrease, respectively, as the actuator volume increases. We track and model chamber volume in this work, however, one might equivalently measure membrane area evolution as a function of time. In Fig. 2d (plus signs) we illustrate the time evolution of the normalized membrane surface area A/A_0, where A and A_0 are the instantaneous and initial membrane area, respectively. These data arise from a surface integral (assuming cylindrical symmetry) of the experimental bulge profile. Using the hyperelastic bulge model developed in Sec. 3.4 reproduces the area response (Fig. 2d, circles) for a series of experimentally determined V/V_0 values from the same conditions Fig. 2c , thereby illustrating the invariance of the results with respect to the chosen observable.

Interestingly, at sufficiently large deformation, the region surrounding the peak of the bulge begins to exhibit color variations, possibly due to interactions with visible light (ESI†, Fig. S11). Predictions of film thickness at an experimentally determined $A/A_0 \sim 12 - 13.5$ suggest the center of the film is on the order of 800-900 nm, just above the wavelength of visible light. We leave this observation for future exploration.

3.2 Modeling Volumetric Flow Rate and Permeability

In this section, we develop the first order differential equation describing chamber volume time evolution for arbitrary membrane mechanics. Assumptions include: water potential defined relative to pure water at atmospheric pressure, negligible salt leakage from an ideal solution enclosed in the chamber, and first order Fickian diffusion through the membrane.

3.2.1 Flux Through a Membrane.

Water passes through a silicone membrane via solution-diffusion,[56] meaning that molecules must first dissolve from a reservoir into the membrane and then release from the other side after passing through. Within the membrane, the water obeys Fick's first law, resulting in a linear dependence of volumetric flux J_Q on the driving force across the membrane due to water potential Ψ. Ψ is the sum of the osmotic potential Π and turgor pressure P_t, with $\Pi = -iCRT$ (Van't hoff's law) and $P_t = 0$ at atmospheric pressure. (The solute electronic dissociation factor, solute concentration, universal gas constant, and temperature are represented by i, C, R, and T, respectively.) Thus, volumetric flux [units: $m^3/(m^2 s)$] is given by

$$J_Q \propto -\nabla\Psi = -L\frac{(\Pi + P_t)}{l} \tag{1}$$

where the potential gradient is applied over a film of thickness l and the pure reservoir reference state ($\Psi = 0$) is implicitly accounted for. L is the constant of proportionality that mediates the

potential gradient and in this case is the mobility, which is given by (see ESI†)

$$L = \frac{P_w C_w}{RT}\frac{V_m M_w}{\rho_w}, \tag{2}$$

and defined in terms of the membrane's permeability to water P_w; the solution water concentration C_w; and the molar volume, molecular weight, and mass density of water V_m, M_w, and ρ_w. Permeability includes both solution into and out of the membrane and the diffusive behavior through the membrane and thus is further decomposed into

$$P_w = D_w \cdot K_{\text{w:membrane}} \tag{3}$$

where $K_{\text{w:membrane}}$ defines the sorption or partition coefficient between the reservoir and the membrane [unitless] and D_w is the diffusivity of the water within the membrane [units: m^2/s].

3.2.2 Chamber Volume Evolution

We assume that deflection of the thin membrane encloses a volume ΔV equal to the volume of the water that enters due to fluid incompressibility and negligible deflection of the stiffer, thicker chamber walls. It is convenient to track membrane deformation independent of initial-chamber-geometry using a dimensionless, deflected membrane volume $\tilde{V}$

$$\tilde{V} = \frac{\Delta V}{A_0 a} = \frac{V - V_0}{A_0 a} = \frac{\frac{V}{V_0} - 1}{\frac{A_0 a}{V_0}} \tag{4}$$

as chamber turgor pressure, membrane thickness, and membrane area vary naturally with $\tilde{V}$ according to the membrane's constitutive behavior only (rather than V_0). The instantaneous rate of change in chamber volume $\frac{dV}{dt}$ due to volumetric water flux J_Q is therefore

$$\frac{dV}{dt} = \iint_{A(\tilde{V})} J_Q(\tilde{V})\ dS \tag{5}$$

where $A(\tilde{V})$ denotes the area of the surface S over which $\tilde{V}$-dependent flux is integrated. Eqn. (1) illustrates that J_Q's dependence on $\tilde{V}$ arises via Π, P_t, and l. The first two terms, Π and P_t are uniform within the chamber due to its being well-mixed and under hydrostatic pressure, respectively. The potential for flow due to osmotic pressure decreases as a function of the increasing chamber volume, $\Pi = \Pi_0 \frac{V_0}{V}$, where $\Pi_0 = -iC_0RT$ and C_0 is the initial osmolyte concentration. P_t's dependence on $\tilde{V}$ will be addressed in Sections 3.3 and 3.4. The film thickness l varies across the deformed surface and in general cannot be treated as an average value (ESI†). The time-dependent chamber volume change therefore becomes

$$\frac{dV}{dt} = -L\left(\Pi_0\left(\frac{V_0}{V}\right) + P_t(\tilde{V})\right)\iint_{A(\tilde{V})}\frac{1}{l(\tilde{V})}\ dS \tag{6}$$

We recognize the integral term as being $A\langle 1/l\rangle$ (where $\langle\cdot\rangle$ denotes the expectation value). Substituting this relation and nondimensionalizing Eqn. (6) for all variables except time, yields

$$\frac{d\frac{V}{V_0}}{dt} = -\frac{L\Pi_0 A_0}{l_0 V_0}\frac{A(\tilde{V})}{A_0}\left\langle\frac{l_0}{l(\tilde{V})}\right\rangle\left(\frac{1}{\frac{V}{V_0}} + \frac{P_t(\tilde{V})}{\Pi_0}\right) \tag{7}$$

which motivates the definition of three dimensionless expressions characterizing membrane deflection mechanics: $f_A(\tilde{V}) = \frac{A(\tilde{V})}{A_0}$, $f_l(\tilde{V}) = \left\langle\frac{l_0}{l(\tilde{V})}\right\rangle$, and $f_p(\tilde{V}) = \frac{P_t(\tilde{V})}{E}$. (We use Young's modulus E to nondimensionalize turgor pressure P_t.) Re-writing Eqn. (7) with these functions gives the final result for the time-dependent, instantaneous dimensionless volume change of the actuating chamber

$$\frac{d\frac{V}{V_0}}{dt} = -\frac{L\Pi_0 A_0}{l_0 V_0} f_A(\tilde{V}) f_l(\tilde{V})\left(\frac{1}{\frac{V}{V_0}} + \frac{E f_p(\tilde{V})}{\Pi_0}\right), \tag{8}$$

where $\tilde{V}$ and V/V_0 are related according to Eqn. (4). This form suggests that an appropriate time constant for the system is:

$$\tau = -\frac{l_0 V_0}{L\Pi_0 A_0}. \tag{9}$$

For a given mechanical response (f_A, f_l, and f_p) and water mobility L within the membrane, Eqn. (8) predicts the dimensionless time-dependent response of an actuating chamber as

$$\frac{d\frac{V}{V_0}}{d\tilde{t}} = f_A(\tilde{V}) f_l(\tilde{V})\left(\frac{1}{\frac{V}{V_0}} + \frac{E f_p(\tilde{V})}{\Pi_0}\right). \tag{10}$$

3.3 Linear Elastic Membrane Bulge Theory

Assuming linear elasticity as a simple starting point provides some insight into the dimensionless functions' f_A, f_l, and f_p dependence on $\tilde{V}$. As we will show, this small strain assumption is poor for most of the observed deformation and in the next section, we provide the more complex, hyperelastic description.

An expression for chamber turgor pressure arises from the combination of Timoshenko's linear elastic cylindrical membrane bulge theory[57] and the Nix approximation[58] connecting the deflection distance to the deflected volume using. Using a spherical cap approximation provides a reasonable estimate of the deflected membrane's surface area for a given deflection distance.[13] Combined with an assumption that under small deformation, the membrane exhibits negligible changes in thickness, these relations yield the following expressions (See ESI† for details):

$$f_p(\tilde{V}) = \frac{P_t(t)}{E} = \frac{128\pi^2}{3}\frac{l_0}{A_0^5}(V(t) - V_0)^3 = \frac{128}{3}\frac{l_0}{a}\tilde{V}^3 \tag{11}$$

$$f_A(\tilde{V}) = \frac{A(t)}{A_0} = 1 + \frac{4(V(t) - V_0)^2}{a^4} = 1 + 4\pi\tilde{V}^2 \tag{12}$$

$$f_l(\tilde{V}) = \frac{l_0}{l(\tilde{V})} = \frac{l_0}{l_0} = 1 \tag{13}$$

Shown gold lines in Fig. 3 a, b, and c, the linear approximation predicts an overly stiff membrane response with volume change, only agreeing with the hyperelastic response at the lowest values of deflection, $\tilde{V} < 0.05$ (saturated gold region). This level of deflection corresponds approximately to an average biaxial stretch within the membrane of $\overline{\lambda} = \sqrt{A/A_0} \sim 1.2$.

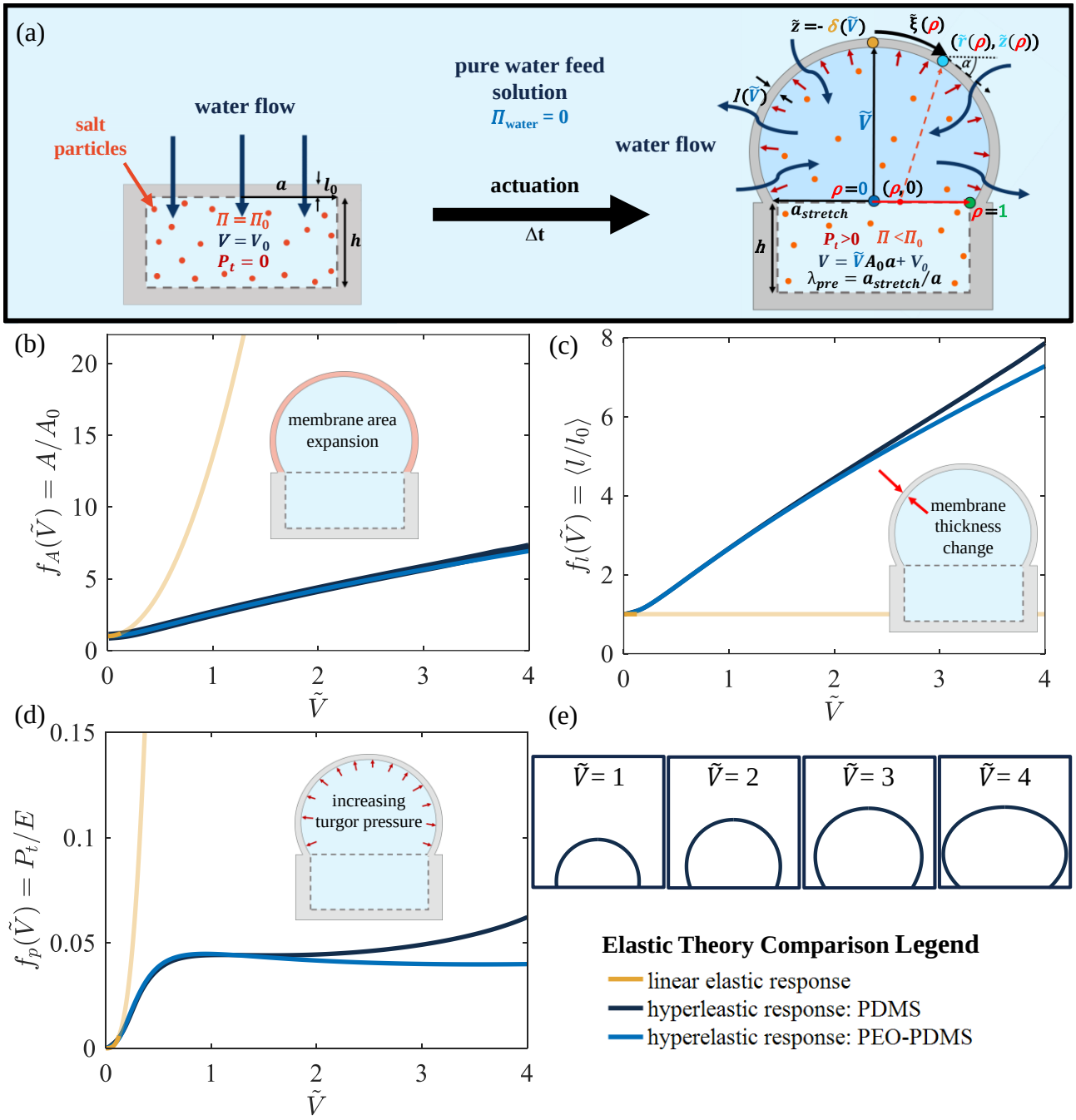

Fig. 3 Mechanical model of bulging membrane. (a) Water enters the chamber through the selectively permeable membrane, driven by the initial osmotic pressure Π_0. The membrane deflects along the -$\tilde{z}$-axis to a maximum of $-\delta$ while developing turgor pressure P_t. Equilibrium membrane geometry is parameterized by ρ, the initial radial position in the undeformed configuration which stretches to a dimensionless arc length $\tilde{\xi}(\rho)$ for deformed coordinates $\tilde{r}(\rho)$ and $\tilde{z}(\rho)$. For reference chamber conditions, three dimensionless functions characterize the bulged membrane area (b), inverse thickness (c), and turgor pressure (d) as a function of dimensionless bulge volume $\tilde{V}$. Three constitutive responses are shown: linear elastic with an equivalent modulus (gold; light gold beyond the small stretch regime), hyperelastic PDMS (navy), and hyperelastic PEO-PDMS (light blue). (Hyperelasticity details in Sec. 3.4.) (e) The bulge deformation profile of a hyperelastic PDMS membrane in the reference geometry illustrates the shape evolution across $\tilde{V} = (0,4)$. All curves set $\lambda_{\text{pre}} = 1$.

3.4 Hyperelastic Membrane Mechanics

To capture large membrane deformation, we use a hyperelastic bulge model[53,59] to define $f_A(\tilde{V})$, $f_l(\tilde{V})$, and $f_p(\tilde{V})$. We treat the membrane as an incompressible Gent 3-parameter material[60] with strain energy density function,

$$W = -C_1 J_m \ln\left(1 - \frac{J_1}{J_m}\right) + C_2 \ln\left(\frac{J_2 + 3}{3}\right), \tag{14}$$

expressed in terms of the first and second strain invariants J_1 and J_2, defined as

$$J_1 = \lambda_\xi^2 + \lambda\phi^2 + \frac{1}{\lambda_\xi \lambda\phi}^2 - 3, \tag{15}$$

$$J_2 = \lambda_\xi^{-2} + \lambda\phi^{-2} + \frac{1}{\lambda_\xi \lambda\phi}^{-2} - 3. \tag{16}$$

This model captures the mechanical response of the membrane materials using parameters fit from both mechanical characterization geometries. Uniaxial tensile data are available in the ESI†. The resulting fit parameters, combined with the following equations, capture the experimentally observed deformation (Fig. 1, dark-blue lines).

3.4.1 Deformed Membrane Profile.

We determine the membrane deformation profile guided by the work of Long, *et al.*[53] who combine governing equations describing the deformation of a hyperelastic cylindrical cap[59] with clamped boundary conditions at the cylinder edge. Throughout, we use their definitions for parameters, but nondimensionalized with respect to length using the initial membrane radius a (*e.g.*, $\tilde{r} = r/a$, $\tilde{z} = z/a$). These variables are illustrated in Fig. 3a. The membrane is parameterized using ρ, $0 \le \rho \le 1$, with the undeformed radial membrane profile lying along the $\tilde{r}$-axis at $\tilde{z} = 0$ from $\rho = 0$ at $\tilde{r} = 0$ to $\rho = 1$ at $\tilde{r} = 1$. The deformed membrane coordinates are expressed as functions the parameter ρ as ($\tilde{r}(\rho)$, $\tilde{z}(\rho)$). Each position on the deformed profile is associated with an arc-length $\tilde{\xi}(\rho)$, where the initial point $\tilde{\xi}(\rho) = 0$ occurs at $\rho = 0$. The angle formed by the tangent line to each deformed point is $\alpha(\rho)$. In the deformed state, the membrane experiences principal stretch ratios $\lambda_\xi(\rho)$, $\lambda_\phi(\rho)$, and $\lambda_r(\rho)$ at each position ρ. The longitudinal and latitudinal stretches are defined, respectively, as

$$\lambda_\xi(\rho) = \frac{d\tilde{\xi}}{d\rho} \qquad \lambda_\phi(\rho) = \frac{\tilde{r}}{\rho}, \tag{17}$$

and the assumption of membrane incompressibility requires $\lambda_r(\rho)$, the stretch ratio related to the dimensionless change in membrane thickness, to be:

$$\lambda_r(\rho) = \frac{1}{\lambda_\xi(\rho)\lambda_\phi(\rho)} = \frac{l(\rho)}{l_0}. \tag{18}$$

In an ideal system, changes in P_t deform only the membrane. However, experimentally we observe expansion of the compliant PDMS chamber with increasing P_t (corresponding to increasing $\tilde{V}$). We account for this effect using as an experimentally measured radial membrane pre-stretch, $\lambda_{\text{pre}}(\tilde{V})$ (ESI† Fig. S6).

Boundary conditions capture 1) the fixed $\tilde{z}$ of the membrane edge, 2) the stretch ratio at the fixed edge (equal to λ_{pre}), 3) a constant encapsulated bulge volume, and 4) an assumption of radial symmetry. These are expressed as

$$\tilde{z}(\rho = 1) = 0$$

$$\lambda_\phi(\rho = 1) = \lambda_{pre}$$

$$\tilde{V}(\rho = 0) = 0 \qquad \tilde{V}(\rho = 1) = \tilde{V}$$

$$\lambda_\xi(\rho = 0) = \lambda_\phi(\rho = 0) \qquad \alpha(\rho = 0) = 0$$

respectively, where the latter reflect the equibiaxial extension and horizontal tangent line at the membrane's center. These boundary conditions limit solutions to physically-relevant deformation profiles for a given turgor pressure. We found that fixed bulge volume was critical to modeling strain stiffening materials, as opposed to fixed deflection at $\tilde{z} = 0$, because the latter does not provide a unique solution as the bulge begins to flatten at large deformations.

Labai and Simmonds[59] derived the static equilibrium and geometric relationships to describe membrane deformation under the application of uniform pressure P_t. For the Gent 3-parameter constitutive model, the natural nondimensionalization of the turgor pressure is $\tilde{P}_t = \frac{P_t a}{C_1 l_0}$. Using this dimensionless parameterization, Labai and Simmonds equations, and a differential form for determining the volume $\tilde{V}$ from the membrane profile (a function of ρ, λ_ϕ, and $\tilde{z}$), we define 5 governing equations,

$$\frac{d\lambda_\xi}{d\rho} = \frac{\lambda_\xi(\tilde{T}_\phi - \tilde{T}_\xi)\cos\alpha - \lambda_\phi \frac{\partial \tilde{T}_\xi}{\partial \lambda_\phi}(\lambda_\xi \cos\alpha - \lambda_\phi)}{\rho\lambda_\phi \frac{\partial \tilde{T}_\xi}{\partial \lambda_\xi}} \tag{19}$$

$$\frac{d\alpha}{d\rho} = \frac{\tilde{P}_t \rho \lambda_\phi \lambda_\xi - \lambda_\xi \tilde{T}_\phi \sin\alpha}{\rho\lambda_\phi \tilde{T}_\xi} \tag{20}$$

$$\frac{d\lambda_\phi}{d\rho} = \frac{\lambda_\xi \cos\alpha - \lambda_\phi}{\rho} \tag{21}$$

$$\frac{d\tilde{z}}{d\rho} = \lambda_\xi \sin\alpha \tag{22}$$

$$\frac{d\tilde{V}}{d\rho} = \lambda_\phi \rho^2 \frac{d\tilde{z}}{d\rho} \tag{23}$$

where the dimensionless line tensions in the ξ and ϕ directions are given as derivatives of the strain energy density function W, and nondimensionalized by the Gent-parameter, C_1:

$$\tilde{T}_\xi = \frac{1}{C_1\lambda_\phi}\frac{\partial W}{\partial \lambda_\xi} \qquad \tilde{T}_\phi = \frac{1}{C_1\lambda_\xi}\frac{\partial W}{\partial \lambda_\phi}. \tag{24}$$

We solve this set of ordinary differential equations (ODEs) by integrating over $0 \le \rho \le 1$ and enforcing the described boundary conditions, using the MATLAB boundary value solver BVP5C. For a given deformed volume $\tilde{V}$, we solve for the dimensionless pressure $\tilde{P}_t$ required to deform the membrane and the parameters defining the membrane geometry $\lambda_\xi(\rho)$, $\alpha(\rho)$, $\lambda_\phi(\rho)$, $\tilde{z}(\rho)$, and $\tilde{V}(\rho)$ for $0 \le \rho \le 1$. The initial guess is a spherical cap approximating the pressure with that of neoHookean membrane of similar volume.[53] The solution maps to the deformation profile

$(\tilde{r}(\rho), \tilde{z}(\rho))$ via the functions $\tilde{z}(\rho)$ and $\lambda_\phi(\rho)$ with the relation to $\tilde{r}$ given by Eqn. (17). A series of profiles are shown in Fig. 3e.

3.5 From Profile to Membrane Geometry

Each membrane profile corresponds to a unique turgor pressure P_t. Thus, the deformed geometry, as parameterized by the dimensionless volume enclosed by the deflecting membrane $\tilde{V}$, can be linked to P_t, l, and A to define the hyperelastic membrane mechanics functions $f_A(\tilde{V})$, $f_l(\tilde{V})$, and $f_p(\tilde{V})$ required to fully define Eqn. (8). For each 'turgor pressure' - 'deformed profile' pair, we verify the volume enclosed by the membrane profile and calculate the membrane surface area and the average inverse thickness via integration. (See ESI† for details.) For f_l, average inverse thickness is nearly equivalent to the inverse of the average membrane thickness for the constitutive response and loading conditions here (ESI Fig. S1).

Figure 3 provides $\tilde{V}$ dependence for membranes well beyond a hemispherical cap, $\tilde{V} = 2/3$. We include predictions for experimentally-determined constitutive responses from the two material systems considered here: Solaris (navy lines) and PEO-Solaris (light blue lines). For devices such as those we report here, in which the bulging surface serves as *both* actuator and membrane, nearly order-of-magnitude increases in membrane area and inverse thickness (decreased thickness) critically mediate the volumetric flux (Eqn. (8)) for a given driving force $(\Pi + P_t)/\Pi_0$. Pressure, on the other hand increases slowly (or plateaus in the case of PEO-PDMS) meaning that for thin, highly deformable films the evolution of the driving force for flow is primarily mediated by changes in osmotic pressure Π/Π_0, which decreases as $\sim V_0/V = \frac{1}{\tilde{V}\frac{A_0 a}{V_0}+1}$.

The complex nonlinearity of this system therefore arises from both the nonlinear material response and the inherent nonlinearity of the ODE. This presents a challenge to easily understanding how the time-dependent response evolves with changes in chamber/membrane geometry or initial osmotic pressure. As an example, we model the volume evolution using *dimensionless* time (Eqn. (9)) assuming constant $P_w = 2\times10^{-12}$ m^2/s (Fig. 4a) for the experimental conditions in Fig. 2c. The time-dependent response of a reference chamber ($a = 200$ μm, $l_0 = 20$ μm, $C_0 = 3$ M; navy line) is compared to a smaller radius chamber ($a = 100$ μm; orange line), a membrane with larger initial thickness ($l_0 = 26$ μm; gold line), and a chamber containing a lower initial salt concentration or osmotic potential ($C_0 = 1$ M; gray line). Note that in dimensionless time, the reference, thick membrane, and reduced osmotic pressure curves collapse since 1) these variables are accounted for in the definition of $\tilde{t}$ or 2) in the case of the thick membrane, the thickness change is small enough to produce little variation in f_A, f_l, and f_p. Fig. 4b shows that in the case of the small chamber the faster relative response time arises from increased geometric changes, $f_A \times f_l = \left(\frac{A}{A_0}\right) \times \left\langle \frac{l_0}{l} \right\rangle$, that favor flux and far outpace the rapid loss of driving force $\frac{\Pi+P_t}{\Pi_0}$ that accompanies this chamber size.

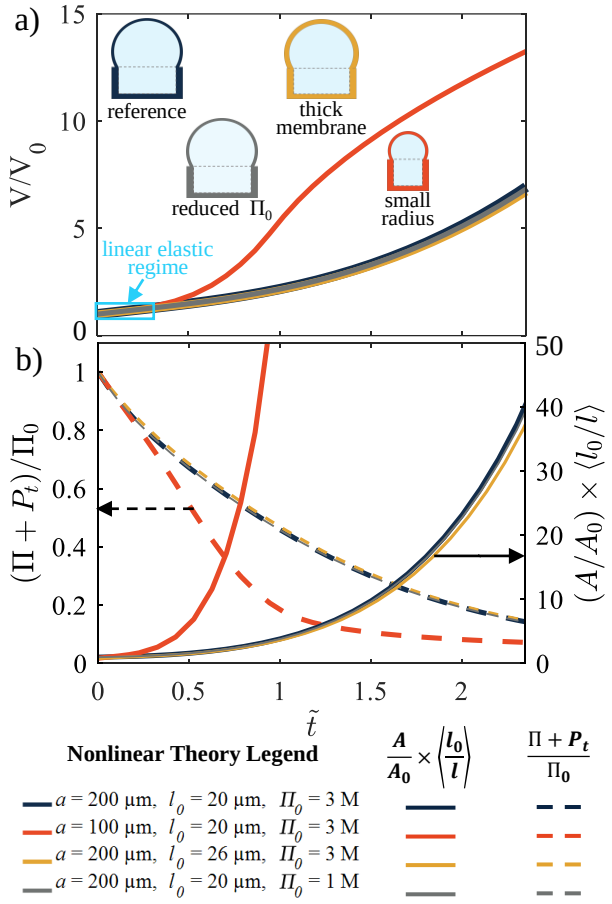

Fig. 4 Predicted time-evolution of chamber volume incorporating large deformation and flux governed by membrane geometry evolution. (a) In dimensionless time $\tilde{t}$ the evolution of chamber volume $\frac{V}{V_0}$ collapses for all experimental configurations except the small radius chamber: reference chamber (navy blue), thick membrane chamber (gold), reduced osmotic loading chamber (gray), and small radius chamber (orange). (Assumptions: Solaris PDMS constitutive response membrane and constant permeability P_w.) (b) The small radius chamber exhibits faster relative actuation due to membrane geometry evolution $f_A f_l = A/A_0\langle l_0/l\rangle$ (solid) whose nearly 10^3 increase facilitating flow outpaces the faster, but order 1 loss in flow driving force $(\Pi+P_t)/\Pi_0$ inducing flow.

3.6 The permeability of water through PDMS

Using known experimental conditions and independent, fit-mediated membrane mechanics, the only remaining unknown is the permeability P_w. (Mobility L and P_w are related via molecular constants by Eqn. (2).) In this section, we determine P_w in the linear regime for short times, then illustrate improvement upon incorporating nonlinear mechanical behavior for longer times. However, we find that a constant value for the permeability P_w cannot describe the actuators' time-dependent responses.

In all cases, we fit the solution to Eqn. (10) to experimental data normalized by the time-constant τ (Eqn. (9)) using nonlinear least squares fitting. All following results arise from simultaneous fitting of all geometries and osmotic loading. Differing conditions were also fit separately with no significant variation in P_w.

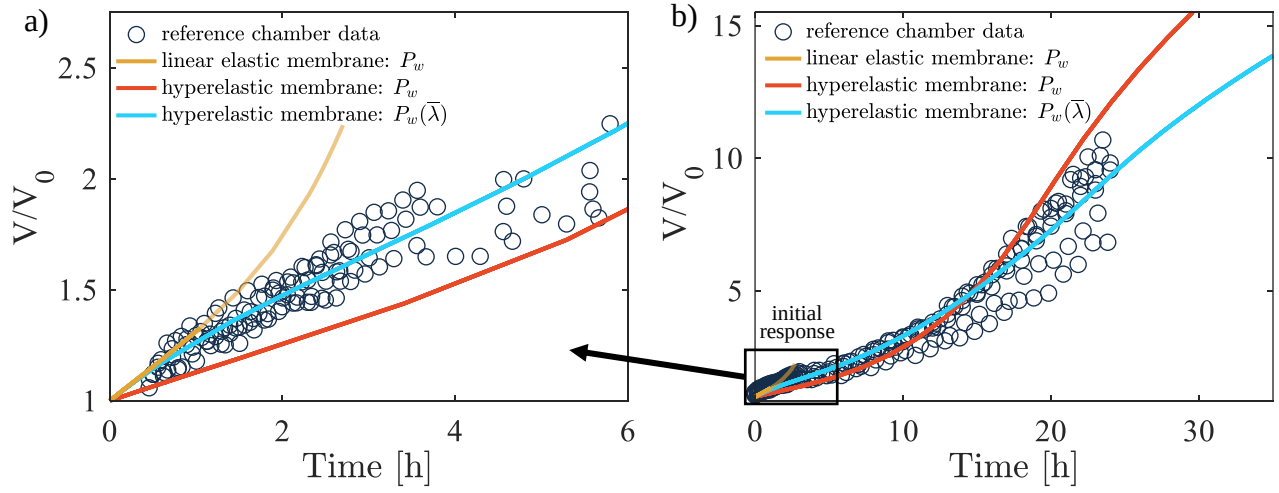

Fig. 5 Fit of experimental data to model. (a) Short- and (b) long-time responses for reference chamber conditions ($a = 200\ \mu$m, $l_0 = 20\ \mu$m, $C_0 = 3$ M) fit to three membrane mechanics/permeability behaviors: linear elastic membrane with constant P_w (gold), hyperelastic membrane with constant P_w (orange), hyperelastic membrane exhibiting stretch-dependent permeability $P_w(\bar{\lambda})$ (teal). The linear elastic response captures the short-time response (dark gold), but overestimates at longer times (light gold extrapolated region). The hyperelastic membrane with constant P_w better captures a moderate stretch response, but underestimates and overestimates at low (a) and high (b) stretches, respectively. A hyperelastic membrane exhibiting stretch-dependent permeability $P_w(\bar{\lambda})$ captures the response (teal) in both regimes (a-b).

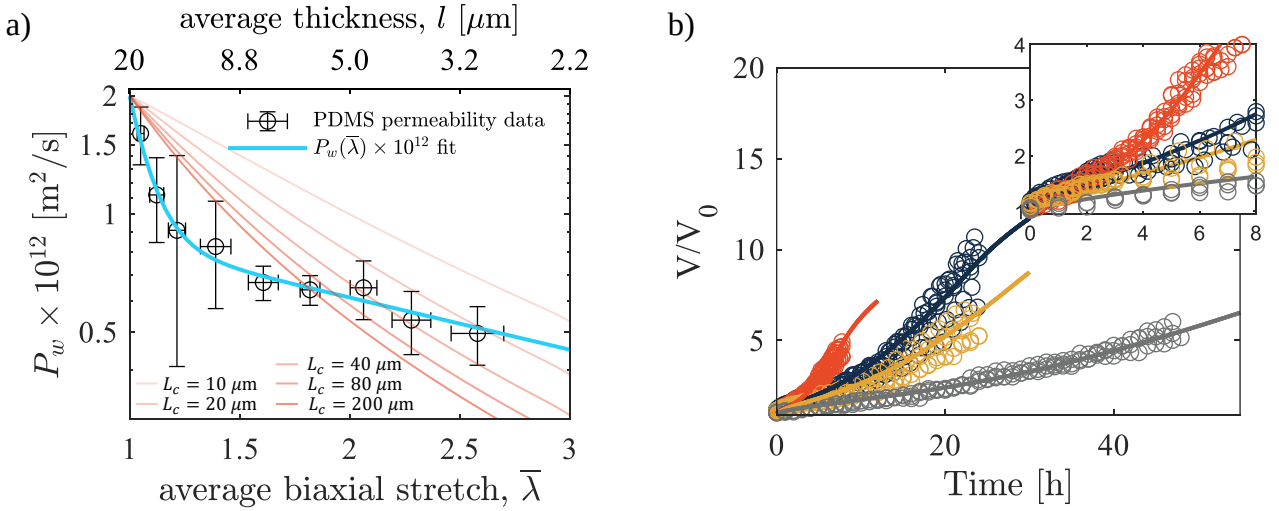

Fig. 6 Deformation-mediated permeability P_w of PDMS. (a) Instantaneous permeability, averaged from all four PDMS chamber conditions, as a function of average biaxial membrane stretch $\bar{\lambda}$ (lower x-axis) and fit to Eqn. (27), teal. Each point (black) represents the average of five instantaneous values, vertical error bars are the standard deviation of the instantaneous permeability values and horizontal error bars are the standard deviation of the average biaxial stretch of each region, where instantaneous permeability values are extracted from segments of 19 experimental $V/V_0(t)$ vs. t curves. This permeability-fit is compared to thickness-dependent (l, upper x-axis) permeability theory expressed by Eqn. (26). Curves for a range of L_c (10-200 μm with increasing orange saturation) capture a significant portion of the deformation-dependent P_w. Each L_c of 10, 20, 40, 80, and 200 μm corresponds to a prediction for $P_{\text{Henry}} \times 10^{12} =$ 3, 4, 6, 10, and 22 mm^2/s. (b) Using deformation-dependent permeability, the model (solid lines) captures the time-dependent actuation of all chambers conditions (circles) at both long and short (inset) times.

Table 2 Permeability values from fit

Constitutive Theory & Fit Employed	Permeability, P_w [m^2/s]
Linear Elastic PDMS	$2.02 \cdot 10^{-12}$
Hyperelastic PDMS, constant P_w	$8.35 \cdot 10^{-13}$
Hyperelastic PDMS, $P_w(\bar{\lambda})$	$1.99 \cdot 10^{-12}$ ($\bar{\lambda} = 1$)
Hyperelastic PEO-PDMS, $P_w(\bar{\lambda})$	$1.99 \cdot 10^{-12}$ ($\bar{\lambda} = 1$)

3.6.1 Linear response permeability

Despite the differences in the experimental responses (Fig. 2), at short times (small deformations) the data collapse in dimensionless time as anticipated (ESI†). Using a slightly extended limit ($\tilde{V} < 0.165$; $V/V_0 < 1.3$ for the reference geometry), which corresponds to an approximate biaxial stretch of 1.4 we obtain the gold line in Fig. 5. (The less saturated color extrapolates the linear prediction.) The permeability value for this regime,

2.02×10^{-12} m^2/s, falls at the upper end of values reported in the literature $6 \times 10^{-13} - 2 \times 10^{-12}$ m^2/s[61–63] (Table 2).

3.6.2 Hyperelastic response - constant permeability

Incorporating the hyperelastic mechanical model captures the middle time (moderate deformation) response, but fails to align with the data at short times and overestimates the highly-stretched response region (20-24 h). Figure 5b (dark orange line) illustrates this result, generally capturing the time-dependent data between 10 and 20 h. However at short times (Fig. 5a, dark orange line), the fit falls well below the experimental observations. As a result, the predicted P_w is 58% lower than measured in the linear regime, although it still lies within the lower range of previously measured values.

3.7 A case for deformation-dependent permeability

Given the accuracy of the membrane mechanical response and known osmotic potential for an experimentally-observed bulge, we conclude that capturing the full, time-dependent response requires a stretch-dependent permeability. We motivate the functional form for the deformation-dependence by piecewise instantaneous permeabilities obtained from multiple actuators/geometries. Instantaneous permeability arises by modifying Eqn. (8) with a deformation-dependent mobility term $L(\tilde{V})$, then re-arranging it to obtain

$$L(\tilde{V}) = -\frac{d\frac{V}{V_0}}{dt}\frac{l_0 V_0}{A_0 \Pi_0}\frac{1}{f_A(\tilde{V}) f_l(\tilde{V})}\frac{1}{\left(\frac{1}{\frac{V}{V_0}} + \frac{E f_p(\tilde{V})}{\Pi_0}\right)} \tag{25}$$

which is a function of the instantaneous chamber volume $\tilde{V}$ and the rate of change of deformation $d(V/V_0)/dt$ (ESI† Fig. S9). $L(\tilde{V})$ is converted to permeability using Eqn. (2). Since membrane deformation, rather than bulge volume, is the likely reason for changes in P_w, we re-express $\tilde{V}$ as the *average* biaxial stretch $\overline{\lambda} = \sqrt{A/A_0}$ (ESI†) and the *average* membrane thickness (dropping the thicker $l_0 = 26$ μm geometry). Fig. 6 illustrates the nearly order-of-magnitude decrease in the membrane permeability during the test.

As membranes become thinner, the flux can become dominated by sorption-desorption surface reaction kinetics.[31,33] Firpo, *et al.*[31] expressed the onset of this thickness-dependent behavior using the concept of a critical thickness value L_c in describing gaseous species permeation through PDMS, where $L_c = 2D_w/k_2$[33] and k_2 is the desorption rate constant. Unfortunately, values of k_2 for liquid water from PDMS appear to be lacking in the literature and reported D_w values may or may not be 'apparent' values depending on the membrane thickness used. Thus, we cannot say definitively where our 20 μm films fall with respect to L_c in this system. However, for context, we can employ the functional form for thickness dependent permeability[31]

$$\frac{P}{P_{\text{Henry}}} = \frac{l/L_c}{1 + l/L_c}, \tag{26}$$

where P_{Henry} represents the permeability of the film in the case that Henry's law applies to the surface reactions, *e.g.*, they are *nearly* in equilibrium. We compare this functional form to our thickness-dependent permeability results to assess the likelihood that our observations arise from a similar mechanism (Fig. 6a).

Although permeability monotonically decreases with decreasing thickness, quantitatively and qualitatively Eqn. (26) provides only moderate agreement with our experimentally observed trend (Fig. 6a). Predictive curves are provided for increasing L_c. We constrain Eqn. (26) to pass through the unstretched state ($\overline{\lambda} = 1$, $P_w = 1.99 \times 10^{-12}$ m^2/s). This choice is supported by the robustness of the collapse of the linear response regime (ESI† Fig. S7) and general agreement with previously reported P_w (2×10^{-12} m^2/s, 55 μm thickness[61,63]). This added constraint leads to a predicted P_{Henry} for each L_c. For large L_c, the curve converges to its maximum thickness sensitivity (close to $L_c = 200$ μm) but predicts an order of magnitude higher P_{Henry} than experimentally measured. (Though it has been simulated for mm-thick films, assuming $K_{\text{w:membrane}} \approx 0.1$.[64]) The lower bound for L_c was motivated by CO_2 and He permeants through PDMS; these are on the order of several 10's of μm's. But such small L_c deviate further from experimental observation. We can speculate on the reasons for the discrepancies between Eqn. (26) and our data.

Two potential reasons for a lack of agreement the deformation-dependent-permeability measurements and thickness-dependent permeability predictions are: 1) treating the membrane thickness as an average value and 2) stretch dependent changes in P_w. Though the thickness of a deformed membrane is not uniform, the majority of the film is within 1 μm of the average value (ESI† Fig. S2). Such small variations in film thickness produce relatively minor variations in the thickness-dependent P_w predicted by Eqn. (26). Using $l \pm 1$ μm to create bounds around the smallest and largest L_c predictions, we determine that qualitatively, our above interpretation does not change (ESI† Fig. S10). Therefore, the curves shown in Fig. 6a provide a reasonable representation of thickness-dependent permeability effects, which is likely the greatest, but not only, contributor to the geometry-dependence of P_w. We conclude that effects of stretch may therefore occur as well, though to our knowledge, no theoretical expression for stretch-dependent membrane permeability exists for a solid, rubbery-network, unswollen material. Typically, rubbery membranes are mounted to a rigid substrate[65] or used with moderately swelling solvents.[39] In the former case, little deformation occurs and in the latter, stretch dependence is attributed to changes in conformation of fluid-filled channels. Given the negligible swelling of PDMS in water, the latter are unlikely to be present. Several possibilities include: 1) polymer chains in a stretched configuration may experience a change in mobility that alters 'hopping'[66–68] and 'cluster formation'[36,61,69] mechanisms, 2) deviations from the incompressibility assumption which may mean a slightly higher P_w due to decreased density, but such thicker membranes could be interpreted as a lower P_w than in reality in the current incompressible approach. Future study is required to understand these more subtle effects.

To quantitatively capture the data trend and facilitate comparison within this and later work, we fit our data to the following

functional form:

$$P_w(\overline{\lambda}) = C_1 \cdot e^{C_2 \cdot \lambda} + C_3 \cdot e^{C_4 \cdot \lambda} \quad (27)$$

Using this stretch dependence in the time-response ODE captures the experimental volumetric actuation behavior across all timescales for all four experimental geometries as shown in Fig. 6b. The initial permeability at $\overline{\lambda} = 1$ for PDMS is 1.99×10^{-12} [m^2/s], within the range of previously published values and recovering the linear elastic limit. The fit constants are provided in Table 3.

3.7.1 Effects of adding hydrophilic groups

With this means of quantifying mechano-permselectivity accurately, we can evaluate the performance of new material formulations. Previous work suggests that increased permeability is possible through the incorporation of hydrophilic groups within the network solid. One group studied the increased sorption of water into PDMS by adding polyethylene glycol (PEG), finding that PEG could increase the uptake of water from 0.1 to 1.4 wt%.[41] Similarly increased hydrophilicity has been reported in PEO-PDMS composites.[54,70] As a proof-of-concept, we test membranes having 0.5 wt% polyethylene oxide (PEO).

Determination of $P_w(\overline{\lambda})$ in the PEO-PDMS follows the same process outlined in Sec. 3.7. PEO-PDMS membranes are tested using the reference geometry ($a = 200$ μm, $l_0 = 20$ μm, $C_0 = 3$ M); Gent model parameters are in the ESI†; $P_w(\overline{\lambda})$ fit (Fig. 7a, dark blue line) parameters are in Table 3. Figure 7 compares the materials.

We find a moderate increase in P_w (Fig. 7a) and stretch at break in the bulge geometry. Interestingly, this improvement was accompanied by degraded uniaxial tensile mechanical properties, namely a 35% decrease in stretch at break (ESI†, uniaxial and bulge geometries, Fig. S4, S5) which was gathered under dry conditions that may provide one explanation for its poor response. The improved P_w means that PEO-PDMS exhibits a faster actuation rate than PDMS, in spite of its slightly stiffer modulus (+51%) which would provide increased turgor pressure resisting flow. The analysis developed here indicates that the permeability of *undeformed* PMDS and PEO-PDMS vary by only 0.02%, producing similar short time responses. At higher membrane stretch values ($\overline{\lambda} = 3$, $V/V_0 = 7.5$), PEO-PDMS membranes exhibit a 56% larger P_w. It may be that the hydrophilic additions produce only a small increase in the equilibrium sorption behavior (evidenced by similar P_w at $\overline{\lambda} = 1$), but decrease L_c (*e.g.*, via larger k_2).

4 Conclusions

We provide a bulge-based method of determining the stretch-dependent permeation behavior of water through elastomeric membranes. At low deformations, these PDMS membranes exhibit permeability values similar to previously published values.[61,62] However, we find a near order of magnitude decrease at large deformations corresponding to stretch-induced membrane thinning and possibly the stretch itself. Capture of the near order-of-magnitude reduction in both membrane thickness and permeability by a non-equilibrium surface reaction model,[31] implies that geometry-changes provide the primary mechanism for permeability decreases as the bulge grows. The deformation-dependent permeability is replicated for a silicon composite material incorporating hydrophilic PEO groups to the network to provide slightly improved mechano-permselectivity properties.

These results rely upon the fidelity of the mechanical model for the highly bulging membrane and nonlinear, hyperelastic constitutive response. Optical profile matching (Fig. 1) and cross-validation of membrane volume and area time-dependent responses (Fig. 2d) provide evidence of the accuracy of both.

More generally, the approach applies to any thin hyperelastic membrane that can be adhered to a substrate of wells immersed in salt solution. New mechano-permselective functional materials may now be quantitatively evaluated. The microstructural features that optimize these two properties remain an area for future research.

Author Contributions

A. Spitzer performed the investigation, data curation, formal analysis, validation, visualization, and writing (Original Draft Preparation and Review & Editing) of the project. S. Hutchens performed the conceptualization, methodology, funding acquisition, formal analysis, supervision, of the project and contributed to the writing (Review & Editing).

Conflicts of interest

There are no conflicts to declare.

Acknowledgements

This material is based upon work supported by the National Science Foundation under Grant No. (1653676). The material presented in this work was carried out in part in the Micro-Nano-Mechanical Systems Cleanroom Laboratory within the Department of Mechanical Science and Engineering at the University of Illinois.

Notes and references

1 J. A. G. Pais and L. M. G. Ferreira, *Desalination*, 2007, **208**, 269–276.
2 A. Zhu, P. D. Christofides and Y. Cohen, *Journal of Membrane Science*, 2009, **344**, 1–5.
3 G. M. Geise, H. B. Park, A. C. Sagle, B. D. Freeman and J. E. McGrath, *Journal of Membrane Science*, 2011, **369**, 130–138.
4 K. Kimura, N. Ogawa and Y. Watanabe, *Water Science and Technology*, 2013, **67**, 1994–1999.
5 M. Becker, G. Kerstiens and J. Schonherr, *Trees*, 1986, **1**, 54–60.
6 E. Steudle, T. Henzler and U. Bayreuth, *Journal of Experimental Botany*, 1995, **46**, 1067–1076.
7 S. Ong, H. Liu and C. Pidgeon, *Journal of Chromatography A*, 1996, **728**, 113–128.
8 C. Maurel, *Annu. Rev. Plant Physiol. Plant Mol. Biol.*, 1997, **48**, 399–429.
9 Y. Tsujimoto, T. Nakagawa and S. Shimizu, *Biochimica et Biophysica Acta - Bioenergetics*, 2006, **1757**, 1297–1300.
10 J. C. Ellory, H. C. Robinson, J. A. Browning, G. W. Stewart,

Table 3 Stretch Dependent Mobility Function Coefficients

Material	C_1 [m^2/s]	C_2	C_3 [m^2/s]	C_4
Solaris	$2.07 \cdot 10^{-8}$	−9.79	$1.13 \cdot 10^{-12}$	−0.31
PEO-Solaris	$4.85 \cdot 10^{-10}$	−6.27	$1.33 \cdot 10^{-12}$	−0.21

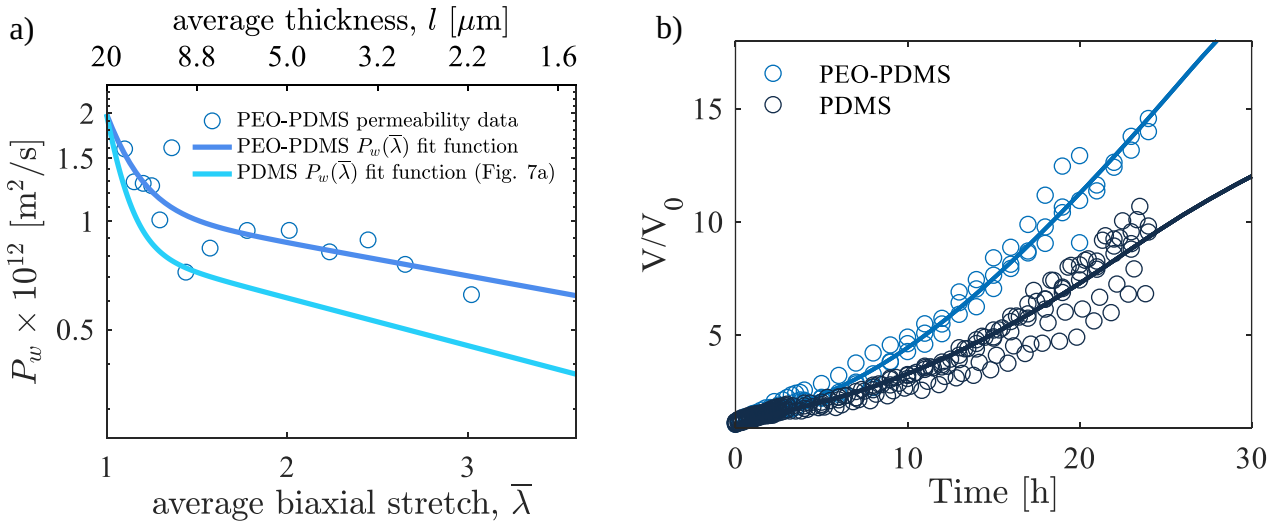

Fig. 7 Comparison of PEO-PDMS and PDMS stretch-dependent permeability $P_w(\overline{\lambda})$. (a) P_w of PEO-PDMS membranes (data: blue circles; fit: dark blue line; chamber conditions: $a = 200$ μm, $l_0 = 20$ μm, $C_0 = 3$ M) exhibit a higher overall permeability than in PDMS (teal line from Fig. 6). Data are the result of three actuating chambers. (b) Accurate modeling of membrane mechanical and permeability properties demonstrate unequivocably that the faster actuation rate of the PEO-PDMS chamber (light blue) arises from permeability and not simply from a difference in constitutive behavior. Both membranes use the reference chamber configuration.

K. A. Gehl and J. S. Gibson, *Blood Cells, Molecules, and Diseases*, 2007, **39**, 1–6.

11 W. Shinoda, *Biochimica et Biophysica Acta - Biomembranes*, 2016, **1858**, 2254–2265.

12 Y. C. Su and L. Lin, *Journal of Microelectromechanical Systems*, 2004, **13**, 75–82.

13 E. Sinibaldi, G. L. Puleo, F. Mattioli, V. Mattoli, F. Di Michele, L. Beccai, F. Tramacere, S. Mancuso and B. Mazzolai, *Bioinspiration and Biomimetics*, 2013, **8**, 025002.

14 E. Sinibaldi, A. Argiolas, G. L. Puleo and B. Mazzolai, *PLoS ONE*, 2014, **9**, 102461.

15 H. Yuk, S. Lin, C. Ma, M. Takaffoli, N. X. Fang and X. Zhao, *Nature Communications*, 2017, **8**, year.

16 H. Hsu, L. Y. Liu, L. Y. Liu and Y. C. Su, *Smart Materials and Structures*, 2018, **27**, 084006.

17 I. Must, E. Sinibaldi and B. Mazzolai, *Nature Communications*, 2019, **10**, 1–8.

18 A. Kataruka and S. B. Hutchens, *Matter*, 2021, **4**, 3991–4005.

19 H. Na, Y. W. Kang, C. S. Park, S. Jung, H. Y. Kim and J. Y. Sun, *Science*, 2022, **376**, 301–307.

20 M. Schanz, *Applied Mechanics Reviews*, 2009, **62**, year.

21 M. L. Oyen, *International Materials Reviews*, 2014, **59**, 44–59.

22 D. Caccavo, S. Cascone, G. Lamberti and A. A. Barba, *Chem. Soc. Rev.*, 2018, **47**, 2357.

23 A. M. Reeve, M. P. Nash, A. J. Taberner and P. M. F. Nielsen, *Journal of Biomechanical Engineering*, 2014, **136**, 1–9.

24 D. Sachs, A. Wahlsten, S. Kozerke, G. Restivo and E. Mazza, *Biomechanics and Modeling in Mechanobiology*, 2021, **20**, 969–982.

25 Y. Leng, M. D. Lucio and H. Gomez, *Computer Methods in Applied Mechanics and Engineering*, 2021, **384**, 113919.

26 J. Wijmans and R. Baker, *Journal of Membrane Science*, 1995, **107**, 1–21.

27 Y. J. Lin, P. Dias, H. Y. Chen, A. Hiltner and E. Baer, *Polymer*, 2008, **49**, 2578–2586.

28 I. Özen, G. Bozoklu, C. Dalgiçdir, O. Yücel, E. Ünsal, M. Çakmak and Y. Z. Menceloğlu, *European Polymer Journal*, 2010, **46**, 226–237.

29 S. Sato, M. Suzuki, S. Kanehashi and K. Nagai, *Journal of Membrane Science*, 2010, **360**, 352–362.

30 P. Peng, B. Shi, Y. Lan, P. Peng, B. Shi and Y. Lan, *Separation Science and Technology*, 2011, **6395**, 234–246.

31 G. Firpo, E. Angeli, L. Repetto and U. Valbusa, *Journal of Membrane Science*, 2015, **481**, 1–8.

32 P. Bian, Y. Wang and T. J. McCarthy, *Macromolecular Rapid Communications*, 2021, **42**, 1–5.

33 M. A. Islam, H. Buschatz and D. Paul, *Journal of Membrane Science*, 2002, **204**, 379–384.

34 M. Muller and V. Abetz, *Chemical Reviews*, 2021, **121**, 14189–14231.

35 B. J. Zwolinski, H. Eyring and C. E. Reese, *Journal of Physical and Colloid Chemistry*, 1949, **53**, 1426–1453.

36 Y. Tamai, *Macromolecules*, 1994, **27**, 4498–4508.

37 C. S. Vidmar, M. Bazzi and V. K. Lai, *Journal of the Mechanical*

Behavior of Biomedical Materials, 2022, **128**, 105107.
38 M. S. Chun and D. Y. Lee, *Bulletin of the Korean Chemical Society*, 2015, **36**, 269–275.
39 R. Song, H. A. Stone, K. H. Jensen and J. Lee, *Journal of Fluid Mechanics*, 2019, 742–754.
40 S. Lee, H.-y. Lee, I.-f. Lee and C.-y. Tseng, *European Journal of Physics*, 2004, **25**, 331–336.
41 A. I. Panou, K. G. Papadokostaki, P. A. Tarantili and M. Sanopoulou, *European Polymer Journal*, 2013, **49**, 1803–1810.
42 M. P. Milner, L. Jin and S. B. Hutchens, *Soft Matter*, 2017, **13**, 6894–6904.
43 A. Souza, E. Marques, C. Balsa and Joao Ribeiro, *applied sciences*, 2020, **10**, 3322.
44 B. Zhang and S. B. Hutchens, *Soft Matter*, 2021, **17**, 6728–6741.
45 E. Yang, M. Zhang, J. Zeng and F. Tian, *Soft Matter*, 2022, **18**, 5465–5473.
46 K. Song, N.-K. Cho, K. Park and C.-S. Kim, *Polymers*, 2022, **14**, 2373.
47 M. Darestani, J. Locq and G. J. Millar, *Separation Science and Technology (Philadelphia)*, 2019, **54**, 128–142.
48 D. C. Pamplona and D. E. Mota, *International Journal of Mechanical Sciences*, 2012, **65**, 18–23.
49 T. Gopesh and J. Friend, *Soft Robotics*, 2021, **8**, 365–370.
50 A. Das, K. S. Breuer and V. Mathai, *Applied Physics Letters*, 2020, **116**, year.
51 M. Sasso, G. Palmieri, G. Chiappini and D. Amodio, *Polymer Testing*, 2008, **27**, 995–1004.
52 A. P. Selvadurai and M. Shi, *International Journal of Non-Linear Mechanics*, 2012, **47**, 228–239.
53 R. Long, K. R. Shull and C. Y. Hui, *Journal of the Mechanics and Physics of Solids*, 2010, **58**, 1225–1242.
54 D. B. Thompson, A. S. Fawcett and M. A. Brook, Silicon Based Polymers: Advances in Synthesis and Supramolecular Organization, 2008, pp. 29–38.
55 Y. Xia and G. M. Whitesides, *Annu. Rev. Mater. Sci*, 1998, **28**, 153–84.
56 J. A. Barrie and D. Machin, *Journal of Macromolecular Science, Part B*, 1969, **3**, 645–672.
57 S. Timoshenko and S. Woinowsky-Krieger, *Theory of plates and shells*, McGraw-Hill, 1959, p. 580.
58 J. J. Vlassak and W. D. Nix, *J. Mater. Res*, 1992, **7**, 3242–3249.
59 A. Libai and J. Simmonds, *The Nonlinear Theory of Elastic Shells*, Cambridge University Press, New York, 1998.
60 A. N. Gent, *International Journal of Non-Linear Mechanics*, 2005, **40**, 165–175.
61 J. M. Watson and M. G. Baron, *Journal of Membrane Science*, 1996, **110**, 47–57.
62 G. C. Randall and P. S. Doyle, *PNAS*, 2005, **102**, 10813–10818.
63 S. J. Harley, E. A. Glascoe and R. S. Maxwell, *Journal of Physical Chemistry B*, 2012, **116**, 14183–14190.
64 C. Lu, Y. Sun, S. Harley and E. Glascoe, *TOUGH Symposium 2012*, 2012, 8.
65 H. Held and S. Landi, *Journal of Biological Standardization*, 1977, **5**, 111–119.
66 R. M. Sok, H. J. Berendsen and W. F. Van Gunsteren, *The Journal of Chemical Physics*, 1992, **96**, 4699–4704.
67 J. J. Lange, C. T. Culbertson and D. A. Higgins, *Analytical Chemistry*, 2008, **80**, 9726–9734.
68 A. E. Ismail, G. S. Grest, D. R. Heine and M. J. Stevens, *Marcomolecules*, 2009, **42**, 3186–3194.
69 J. A. Barrie and B. Platt, *Polymer*, 1963, **4**, 303–313.
70 B. K. D. Ngo, K. K. Lim, S. J. Stafslien and M. A. Grunlan, *Polymer Degradation and Stability*, 2019, **163**, 136–142.